Physica Medica 64 (2019) 24–28

Contents lists available at ScienceDirect

Physica Medica

journal homepage: www.elsevier.com/locate/ejmp

Technical note

Automatic gas detection in prostate cancer patients during image-guided radiation therapy using a deep convolutional neural network

Hideharu Miura[a,b,*], Shuichi Ozawa[a,b], Yoshiko Doi[a,b], Minoru Nakao[a,b], Keiichi Ohnishi[a], Masahiro Kenjo[a,b], Yasushi Nagata[a,b]

[a] Hiroshima High-Precision Radiotherapy Cancer Center, Hiroshima, Japan
[b] Department of Radiation Oncology, Institute of Biomedical & Health Science, Hiroshima University, Hiroshima, Japan

ARTICLE INFO

Keywords:
Deep convolutional neural network
Prostate
Intestinal/rectal gas
Image-guided radiation therapy
Segmentation

ABSTRACT

Purpose: The detection of intestinal/rectal gas is very important during image-guided radiation therapy (IGRT) of prostate cancer patients because intestinal/rectal gas increases the inter- and intra-fractional prostate motion. We propose a deep convolutional neural network (DCNN) to detect intestinal/rectal gas in the pelvic region.
Material and methods: We selected 300 anterior-posterior kilo-voltage (kV) X-ray images from 30 prostate cancer patients. Thirty images were randomly chosen for a test set, and the remaining 270 images used as the training set. The intestinal/rectal gas was manually delineated on kV X-ray images and segmented. The training images were augmented by applying artificial shifts and fed into a DCNN. The network models were trained to keep the quality of the output image close to the quality of the input image by pooling and upsampling. The training set was used to adjust the parameters of the DCNN, and the test set was used to assess the performance of the model. The performance of the DCNN was evaluated using a fivefold cross-validation procedure. The dice similarity coefficient (DSC) was calculated to evaluate the detection accuracy between the manual contour and auto-segmentation.
Results: The DCNN was trained within approximately 17 min with a time step of 20 s/epoch. The training and validation accuracy of the models after 50 epochs were 0.94 and 0.85, respectively. The average ± standard deviation of the DSC for 30 test images was 0.85 ± 0.08.
Conclusions: The proposed DCNN method can automatically detect the intestinal/rectal gas in kV images with good accuracy.

1. Introduction

Three-dimensional conformal radiation therapy, intensity-modulated radiotherapy (IMRT), and volumetric-modulated arc radiotherapy (VMAT) are more effective curative treatment options for patients with localized adenocarcinoma of the prostate, compared with surgery [1–2]. Gastrointestinal toxicity is the major treatment-related side effect in prostate cancer radiotherapy. The rates of acute and chronic grade (≥2) rectal toxicity increase by dose – increasing from 3 and 5%, to 20 and 21%, respectively [3–5]. A small dose at the rectal wall is a prerequisite for a higher dose delivered to the prostate. Artificial spacing material has been used to decrease the dose to the rectum in the rectoprostatic space [6]. Several investigators have reported the relationship between intrafraction prostate motion and rectal contents, such as residual feces or intestinal gas, and methodologies have been proposed for reducing the rectal content and maintaining consistent rectal volume [7–11]. Clinical studies have shown that differences in rectal filling can lead to a risk of local and biochemical failure and decrease in the risk of the rectal toxicity during prostate cancer radiotherapy [12,13].

Gas production is influenced by the amount of fermentable foodstuff and air that escapes from the small bowel into the colon. Shapes and sizes of intestinal gas differ from day to day. Intestinal/rectal gas largely affects the rectal size and shape, which causes intra/interfraction prostate motion [14–16]. Rectal gas shifts the rectal wall into the higher dose region. Therefore, the detection of intestinal/rectal gas using image-guided radiation therapy (IGRT) in prostate cancer patients, particularly in the rectum region, is an important task. An automatic intestinal/rectal detection system for prostate cancer patients could reduce the workload of therapists, providing a safe and reliable radiotherapy treatment.

Convolutional neural networks (CNNs) have been used to solve

* Corresponding author at: Hiroshima High-Precision Radiotherapy Cancer Center, 3-2-2, Futabanosato, Higashi-ku Hiroshima, 732-0057, Japan.
E-mail address: miura@hiprac.jp (H. Miura).

https://doi.org/10.1016/j.ejmp.2019.06.009
Received 14 March 2019; Received in revised form 4 June 2019; Accepted 17 June 2019
Available online 21 June 2019

challenging tasks such as classification, segmentation, and object detection [17]. Several deep learning methods have been widely studied for organ segmentation tasks in the radiotherapy field [18–21]. For example, Men et al. published a deep dilated convolutional neural network (DDCNN) architecture for segmentation of the clinical target volume (CTV) and organs at risks (OAR), such as the bladder, left and right femoral heads, colon, and intestine, in the planning computed tomography (CT) of rectal cancer. Their proposed DDCNN was in good agreement segment for CTV, bladder, and femoral heads with the radiation oncologist contours. The segmentation accuracy for the intestine and colon was low owing to differences in the shape, volume, intensity, boundary, and location between patients.

We aimed to detect the intestinal/rectal gas of prostate cancer patients using DCNN. The performance of the proposed DCNN gas detection model was compared to that of an observer to determine any differences in the results.

2. Materials and methods

2.1. Image preparation

This study was approved by the Institutional Review Board of Hiroshima University (E-1223). The patients were instructed to empty their bowels and rectum before CT simulation and radiotherapy. All patients were imaged for CT simulation and radiotherapy from a head first supine position in an individualized commercialized thermoplastic cast from the abdomen to the thigh with foot support. All patients were treated on a Vero4DRT (Mitsubishi Heavy Industries, Ltd., Hiroshima, Japan, and Brainlab, Munich, Germany) with an ExacTrac X-ray system. A mean dose of 74 or 78 Gy was prescribed for the planning target volume (PTV) in 37 or 39 fractions for all patients, respectively. The patient position was imaged by following our procedures. During treatment, the patient was initially positioned to the planning CT isocenter based on skin markers with a laser coordination system. After an initial setup, the images were taken by two orthogonal X-ray fluoroscopic units used in the patient setup for bone anatomy registration using an ExacTrac X-ray system. A flat panel detector (FPD) with an image area size of 200 × 200 mm and a pixel size of 0.388 mm was used. The image matrix size was 1024 × 768 pixels. In clinical practice, kV images are acquired simultaneously on irradiation ports at anterior-posterior (AP) and lateral directions. The ExacTrac X-ray system images were obtained with the following conditions: 120 kV, 200 mA, and 10 ms. In this study, we used a 2D planar kV image from an AP direction image (Fig. 1-a). Pre-treatment cone-beam computed tomography (CBCT) images were then obtained, and a three degrees of freedom soft tissue based setup was manually performed by radiation therapists using anatomic structures. After the matching was verified on target registration, radiation was delivered to the patients.

A total of 300 X-ray images were randomly selected from 30 prostate cancer patients who underwent IGRT with a Vero4DRT. Thirty kV-images were randomly selected as the test subjects, with the remaining 270 used as the training subjects. The image label was generated from the manual contour using in-house software and the delineation was double-checked (Fig. 1-b). If a gas contour was found on this slice, it was labeled '1', else it was labelled '0'. These binary mask images were used as the ground truth to train the model. All images were scaled to 256 × 256 pixels before importing to the network. Down sampling is commonly used to reduce the size of data requiring processing. Data augmentation, which applies random horizontal and vertical translations of up to 50 pixels in each spatial dimension, or randomly flips the images, was used to artificially increase the amount of training data. The total number of training slices was approximately 3000. To study the effect of the number of images on the modeling accuracy, different numbers of images were used, namely 300, 500, 1000, 2000, and 3000. After data augmentation, the data was randomly separated into training (80%) and validation (20%) datasets in five folders for cross-validation. The training dataset was input into the DCNN for model training. The performance of the model was assessed using the validation dataset.

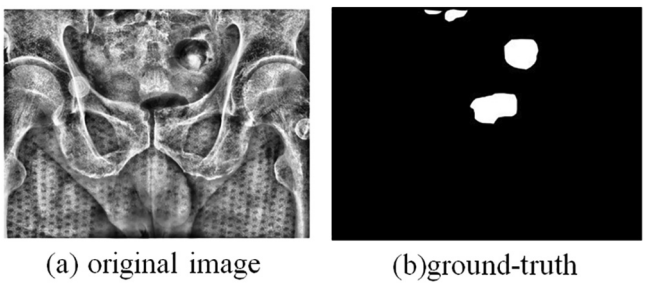

Fig. 1. A sample of (a) kV-X ray image and (b) generated segmentation mask (white: foreground and black: background).

2.2. Network architecture

We used the U-net architecture that was proposed in Ronneberger, et al. [22], whereby a DCNN model can be trained from end-to-end to directly produce a label map for object segmentation in a 2D image. We modified the U-net architecture following a model published by Isola, et al. [23]. These network structures were involved in convolution, leaky rectified linear units (LeakyReLU), batch normalization, dropout, and upsampling layers, as shown in Fig. 2. The down-sampling path has several convolutional layers. Every convolutional layer has a filter size of 2 × 2, stride of 1 in both directions, and LeakyReLU activation, which increases the number of feature maps from 1 to 512 and reduces the feature size from 256 × 256 pixels down to 1 × 1 pixels. In the upsampling path, each deconvolutional layer is filtered to a size of 2 × 2 and stride of 2 × 2, which doubles the size of the feature maps in both directions but decreases the number of feature maps by two, so that the size of feature maps increases from 1 × 1 to 256 × 256. Dropout layers were used to improve the robustness of the network by the random removal of neurons, as well as by reducing the influence of overfitting. In each upsampling path, convolutional layers reduced the number of feature maps of concatenation of deconvolutional feature maps and feature maps from the encoding path. Zero padding was used to keep the output dimensions for all of the convolutional layers of both the downsampling and upsampling paths. A sigmoid layer was used as the final layer. The architecture of the DCNN was implemented in a graphics process unit (GPU) using the publicly available Keras framework [24] and TensorFlow [25] as the backend. The model was trained to minimize the loss function using the Adam optimizer [26]. The learning rate, α, was set to 0.001, and the exponential decay rates β_1 and β_2 were set to 0.9 and 0.999, respectively. To assess the performance of the segmentation procedure, a dice similarity coefficient (DSC) [27] was computed. It was used as an accuracy measure for the training of the proposed DCNN and as a loss function.

The DSC is given by:

$$\mathrm{DSC(A,\ B)} = \frac{2\ |A \cap B|}{|A| + |B|}$$

where A represents the manual delineation, B denotes the auto-detection, and A⋂B is the intersection of A and B. The DSC is represented by a single metric ranging from 0 to 1.0 such that a perfect match would have a DSC of 1.0. The loss was chosen to be the 1-DSC between the automatic and manual gas contours. The test kV X-ray images were fed into the trained DCNN model to detect the intestinal/rectal gas. Our DCNN model was trained for 50 epochs. A GeForce GTX 1080 Ti GPU with 11 GB RAM and 3584 CUDA cores was used for the training.

3. Results

Fig. 3 demonstrates the influence of the sample size on the accuracy

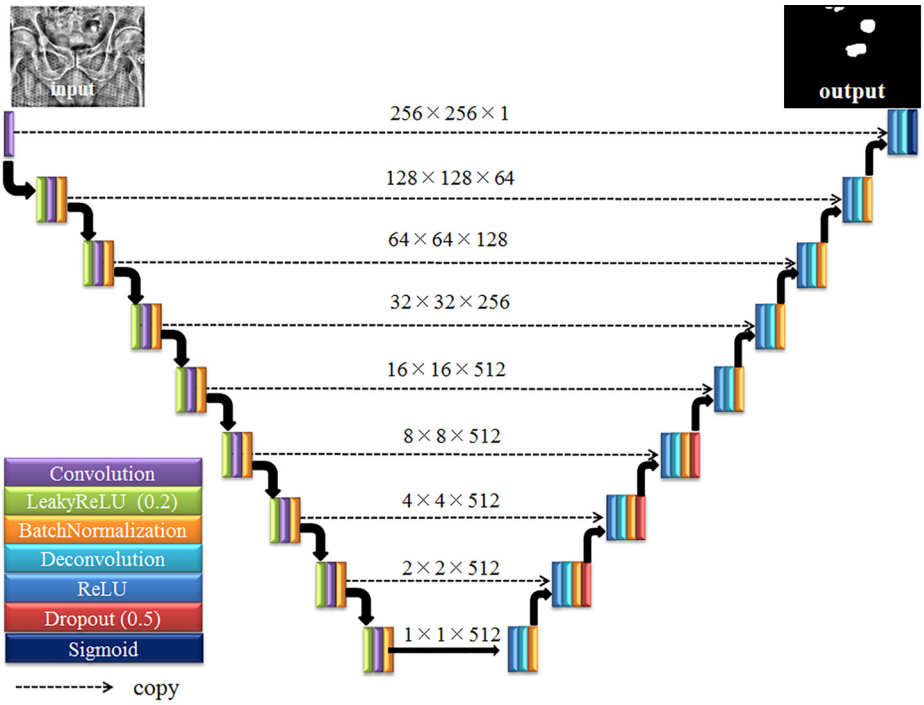

Fig. 2. DCNN consists of the convolution, LeaklyReLU, batch normalization, deconvolution, ReLU, dropout layers, and sigmoid layers. The "M × M × H" labels correspond to the voxel data for the convolutional layers; M is the image size, and H is the number of feature maps. The dashed arrows indicate the feature map copied from the downward path to the upward path.

of our training model. Fig. 3 shows the loss and accuracy of the gas detection using 300, 500, 1000, 2000, and 3000 training samples. At least 1000 images were required to create a model with good accuracy. The training and validation DSCs had similar values at an epoch of 15. After which, the training DSCs gradually increased toward the end of the training process. The validation DSCs rapidly increased and became stable after an epoch of 15. The training and validation accuracy of the models after 50 epochs were 0.94 and 0.85, respectively. The calculation took approximately 17 min for 50 epochs with a time step of 20 s/epoch.

Fig. 4 shows the performance of the model across the 30 image test data cases. The average ± standard deviation of the DSC for 30 test cases was 0.85 ± 0.08. Once the model was trained, it took approximately 30 ms per image to detect the intestinal/rectal gas from a new kV image. The manual- and auto-segmentations of three test data cases are shown in Fig. 5. The auto-segmentations of the gas were close to the manual segmentations in terms of the shapes, sizes, and locations. Fig. 6 shows a poor segmentation using the proposed DCNN. This case was

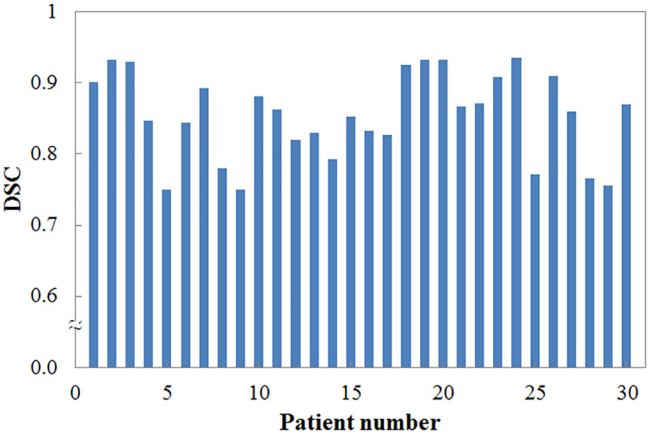

Fig. 4. DSC values for the performance accuracy of gas detection using the proposed DCNN across all patients in the test dataset.

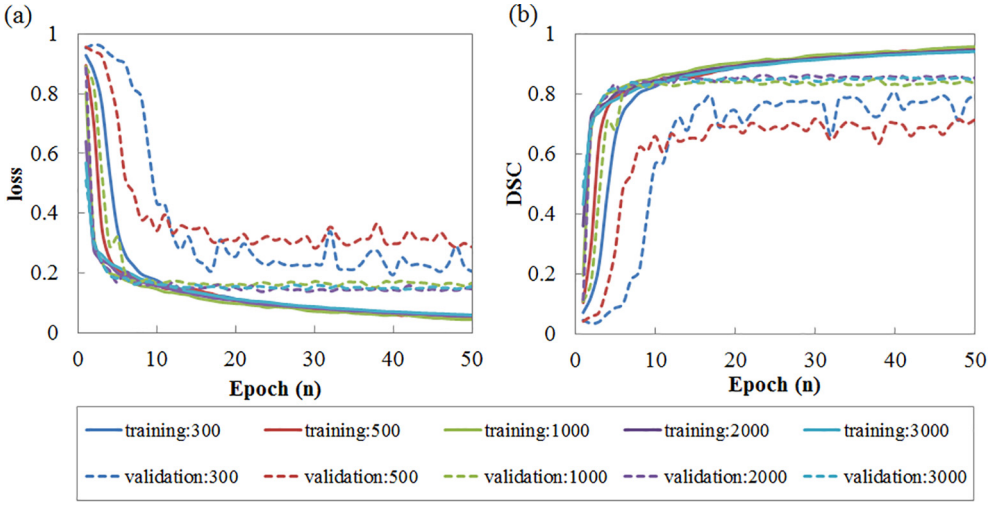

Fig. 3. Plots of the training and validation (a) loss (1-DSC) and (b) accuracy (DSC) as a function of the epochs of different numbers of images.

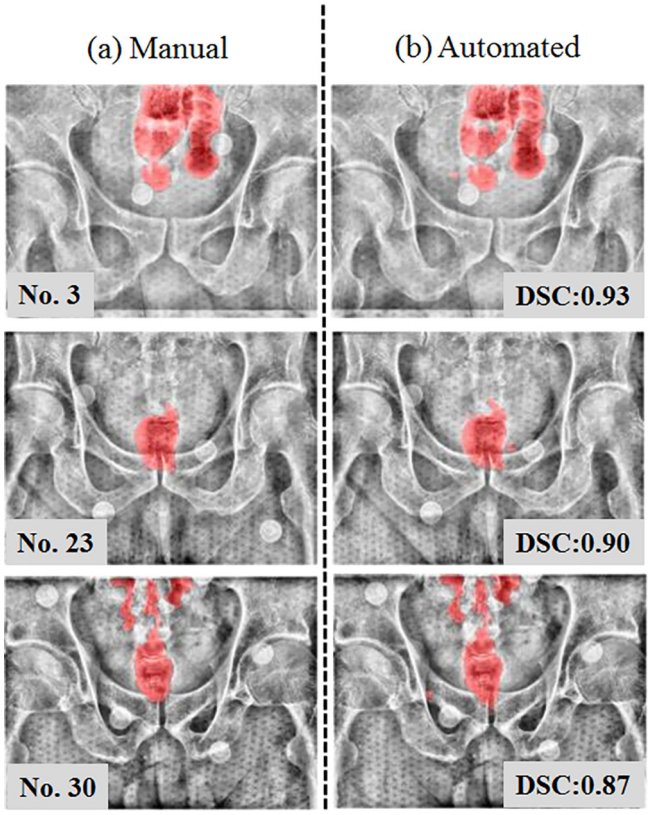

Fig. 5. An example of (a) manual and (b) automated segmentations (the gas area is shown in red). The gas detection time was approximately 30 ms per image. The segmentation results were visually closer to the ground truth. DSC; Dice similarity coefficient. (For interpretation of the references to colour in this figure legend, the reader is referred to the web version of this article.)

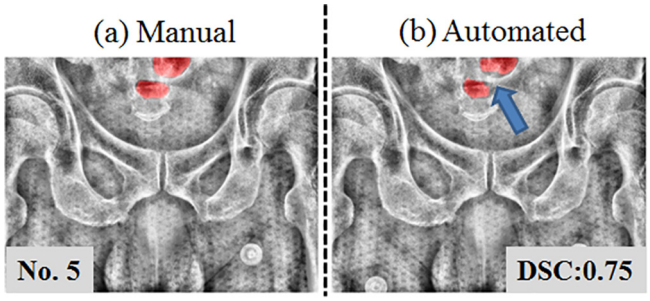

Fig. 6. Example of a poor segmentation image. (a) Manual and (b) automated segmentations (the gas area is shown in red). The undetected area is indicated by a blue arrow. DSC; Dice similarity coefficient. (For interpretation of the references to colour in this figure legend, the reader is referred to the web version of this article.)

worst segmentation, with DSC of 0.75.

4. Discussion

We trained and evaluated a deep framework to segment the gas in IGRT kV images for prostate radiotherapy. Throughout the experiments, we achieved good segmentation results for all of the patients. The DSC of the training demonstrates that the training performance can be further improved, however the validation DSC did not increase, as shown in Fig. 3. This implies that the network began to experience overfitting. Early-stopping should be used to avoid overfitting. Early-stopping is a method that stops training once the model performance stops improving on a holdout validation dataset [28]. We investigated the relationship between the sample size and modeling accuracy. A relatively small image dataset yielded good results for detecting intestinal/rectal gas. Air that is relatively radiolucent on an image will appear black and pale grey. Bone is radiopaque and appears white in an image. Most soft tissues in the body are composed mainly of water and appear as shades of grey. Therefore, intestinal/rectal gas detection for prostate cancer is an easy task because intestinal/rectal gas has large contrast enhancements in kV-planar images. The DSC may decrease slightly because the label of gas sometimes appears as small isolated segments. This problem may be solved by a simple smoothing process (erosion and dilation). The DSC may be too sensitive to small errors when the segmented object is small, and not sensitive enough to large errors when the segmented object is large. Prostate motion is considered to be greater for patients who have gas volumes greater than 0.5 cm^3 [29]. Therefore, small amounts of gas for prostate cancer is not significant.

Stroom et al. discussed gas pocket detection in the rectum for the quantitative determination of the rectum wall and, indirectly, the prostate position using electronic portal imaging [30]. The gas pockets were automatically determined by searching the minimum pixel value, and values below the threshold with all neighboring pixels for the dark spots in a specific region. The search region was limited by the cranial and caudal ends of the prostate because gas pockets appearing outside the sigmoid or anus region did not have an effect on the prostate motion. The amount of air could also be determined based on Hounsfield units (between −10 and −1000) using CT [12]. The kV planar images did not enable the quantification of the gas in the same way that kV-CBCT could because many similar black areas existed on the planar image.

Two on-board imaging modalities are widely used in image-guided radiotherapy for prostate cancer patients: 2D kV orthogonal imaging with fiducial markers and CBCT. The kV orthogonal imaging with fiducial markers has the advantages that only minimal imaging doses are required and there is a reduced image acquisition and alignment time. The kV orthogonal imaging with fiducial markers and daily IGRT for prostate cancer is more precise than CBCT [31]. CBCT visualizes the surrounding OAR, such as the rectum, bladder, and bowel, and requires confirmation that these organs are at least the same size as the simulation. A combined imaging procedure, that includes kV-fiducial marker-based alignment with our proposed gas detection method and CBCT, may be useful for accurate and precise target alignment, while minimizing doses to healthy tissue. The presence of gas in the bowel/rectum induces substantial density variations that may result in a dose distribution for proton therapy [32].

There are several limitations in this study. First, we evaluated the performance of the auto-segmentation algorithm under DSC only. The Hausdorff distance, mean distance to agreement, and Jaccard index can be used to evaluate the performance of the auto-segmentation algorithm. However, the DSC is the most widely used evaluation index in the literature. Second, we only used a simple network structure, which was similar to U-net. This model consists of equal numbers of down- and up-sampling layers to segment the cell structures. Many CNN-based segmentation methods have been used to achieve state-of-the-art performances in different medical image segmentation tasks [33–36]. For example, Kamnitsas et al. proposed a multi-pathway CNN network (DeepMedic) to segment brain lesions [33]. Huang et al. proposed a densely connected convolutional network (Dense-Net) and achieved a state-of-the-art performance in natural image classification and recognition [34]. If the model requires improvement, a more robust model may be possible.

Gas in the rectum may increase the intrafractional internal error. This is still a significant issue in image-guided radiotherapy, whereas interfractional error is largely eliminated due to daily image guidance. The current IGRT is manually performed by a therapist. CyberKnife is equipped with an automated marker tracking system to correct intrafraction prostate motion [37]. Even if gas suddenly appears during

image acquisition, the CyberKnife system cannot immediately stop the treatment to compensate for the rectum gas. Our proposed model was only established to detect intestinal/rectal gas. To alert a therapist when an area exceeds the defined threshold, a warning message can be displayed along with a beeping audio signal. Regions of interest (ROI) should be considered a limited area because the prostate gland is located behind the pubic bone. We do not need gas detection of the whole pelvis region or fine contouring. We only need to check if gas exists around the pubis planar kV images. When a large ROI, including the small intestines, is defined the alarm will sound frequently. Our proposed method would not increase the treatment time because kV 2D planar images are already routinely acquired for setup verification. The long-term goal is to incorporate our proposed model for gas detection into an IGRT. We will investigate the relationship between the gas in kV planar images and prostate motion of daily CBCT using deep learning, and incorporate this into our proposed gas detection system.

5. Conclusions

The detection of intestinal/rectal gas is very important for IGRT of prostate cancer patients. We proposed a DCNN to detect intestinal/rectal gas in prostate cancer patients with kV images.

Declaration of Competing Interest

None.

References

[1] Hamdy FC, Donovan JL, Lane JA, Mason M, Metcalfe C, Holding P, et al. 10-year outcomes after monitoring, surgery, or radiotherapy for localized prostate cancer. N Engl J Med 2016;375:1415–24.

[2] Michalski JM, Yan Y, Watkins-Bruner D, Bosch WR, Winter K, Galvin JM, et al. Preliminary toxicity analysis of 3- dimensional conformal radiation therapy versus intensity modulated radiation therapy on the high-dose arm of the Radiation Therapy Oncology Group 0126 prostate cancer trial. Int J Radiat Oncol Biol Phys 2013;87:932–8.

[3] Al-Mamgani A, van Putten WL, Heemsbergen WD, van Leenders GJ, Slot A, Dielwart MF, et al. Update of Dutch multicenter dose escalation trial of radiotherapy for localized prostate cancer. Int J Radiat Oncol Biol Phys 2008;72:980–8.

[4] Zelefsky MJ, Levin EJ, Hunt M, Yamada Y, Shippy AM, Jackson A, et al. Incidence of late rectal and urinary toxicities after three-dimensional conformal radiotherapy and intensity-modulated radiotherapy for localized prostate cancer. Int J Radiat Oncol Biol Phys 2008;70:1124–9.

[5] Kuban DA, Tucker SL, Dong L, Starkschall G, Huang EH, Cheung MR, et al. Long-term results of the M.D. Anderson randomized dose-escalation trial for prostate cancer. Int J Radiat Oncol Biol Phys 2008;70:67–74.

[6] Hamstra DA, Mariados N, Sylvester J, et al. Continued benefit to rectal separation for prostate radiation therapy: final results of a phase III trial. Int J Radiat Oncol Biol Phys. 2017;97:976–85.

[7] Vanneste BGL, van Wijk Y, Lutgens LC, Van Limbergen EJ, van Lin EN, van de Beek K, et al. Dynamics of rectal balloon implant shrinkage in prostate VMAT: influence on anorectal dose and late rectal complication risk. Strahlenther Onkol 2018;194:31–40.

[8] Wang KK, Vapiwala N, Bui V, Deville C, Plastaras JP, Bar-Ad V, et al. The impact of stool and gas volume on intrafraction prostate motion in patients undergoing radiotherapy with daily endorectal balloon. Radiother Oncol 2014;112:89–94.

[9] den Harder AM, van Gils CH, Kotte AN, et al. Effect of magnesium oxide on interfraction prostate motion and rectal filling in prostate cancer radiotherapy: analysis of a randomized clinical trial. Strahlenther Onkol 2014;190:758–61.

[10] Ghilezan MJ, Jaffray DA, Siewerdsen JH, Van Herk M, Shetty A, Sharpe MB, et al. Prostate gland motion assessed with cine-magnetic resonance imaging (cine-MRI). Int J Radiat Oncol Biol Phys 2005;62:406–17.

[11] van Lin EN, van der Vight LP, Witjes JA, Huisman HJ, Leer JW, Visser AG. The effect of an endorectal balloon and off-line correction on the interfraction systematic and random prostate position variations: a comparative study. Int J Radiat Oncol Biol Phys 2005;61:278–88.

[12] de Crevoisier R, Tucker SL, Dong L, et al. Increased risk of biochemical and local failure in patients with distended rectum on the planning CT for prostate cancer radiotherapy. Int J Radiat Oncol Biol Phys 2005;62:965–73.

[13] Heemsbergen WD, Hoogeman MS, Witte MG, et al. Increased risk of biochemical and clinical failure for prostate patients with a large rectum at radiotherapy planning: results from the Dutch trial of 68 GY versus 78 GY. Int J Radiat Oncol Biol Phys 2007;67:1418–24.

[14] Padhani AR, Khoo VS, Suckling J, et al. Evaluating the effect of rectal distension and rectal movement on prostate gland position using cine MRI. Int J Radiat Oncol Biol Phys 1999;44:525–33.

[15] Roeske JC, Forman JD, Mesina CF, et al. Evaluation of changes in the size and location of the prostate, seminal vesicles, bladder, and rectum during a course of external beam radiation therapy. Int J Radiat Oncol Biol Phys 1995;33:1321–9.

[16] Dawson LA, Mah K, Franssen E, Morton G. Target position variability throughout prostate radiotherapy. Int J Radiat Oncol Biol Phys 1998;42:1155–61.

[17] LeCun Y, Bengio Y, Hinton G. Deep learning. Nature 2015;521(7553):436–44.

[18] Meyer P, Noblet V, Mazzara C, Lallement A. Survey on deep learning for radiotherapy. Comput Biol Med 2018;98:126–46.

[19] Ibragimov B, Xing L. Segmentation of organs-at-risks in head and neck CT images using convolutional neural networks. Med Phys 2017;44:547–57.

[20] Wang J, Lu J, Qin G, Shen L, Sun Y, Ying H, et al. Technical Note: A deep learning-based autosegmentation of rectal tumors in MR images. Med Phys 2018;45:2560–4.

[21] Men K, Dai J, Li Y. Automatic segmentation of the clinical target volume and organs at risk in the planning CT for rectal cancer using deep dilated convolutional neural networks. Med Phys 2017;44:6377–89.

[22] Ronneberger O, Fischer P, Brox T. U-Net: convolutional networks for biomedical image segmentation, MICCAI 2015. Part III, LNCS. 2015; 9351: 234–241.

[23] Isola P, Zhu J, Zhou T, Efros AA, Image-to-image translation with conditional adversarial networks; 2017. arXiv preprint. arXiv:1611.07004.

[24] Deep learning for humans. https://github.com/fchollet/keras.

[25] Kingma D, Ba J. Adam: a method for stochastic optimization. Proc. Int. Conf. Learning Represent. 2014:1–13.

[26] Abadi M, Agarwal A, Barham P, et al. Tensorflow: Large-scale machine learning on heterogeneous distributed systems. arXiv preprint arXiv:160304467. 2016.

[27] Dice LR. Measures of the amount of ecologic association between species. Ecology 1945;26:297–302.

[28] Hoffer E, Hubara I, Soudry D. Train longer, generalize better: closing the generalization gap in large batch training of neural networks. arXiv preprint arXiv:1705.08741, 2017.

[29] Adamson J, Wu Q. Inferences about prostate intrafraction motion from pre- and posttreatment volumetric imaging. Int J Radiat Oncol Biol Phys 2009;75:260–7.

[30] Stroom JC, Kroonwijk M, Pasma KL, et al. Detection of internal organ movement in prostate cancer patients using portal images. Med Phys 2000;27:452–61.

[31] Goff PH, Harrison LB, Furhang E, Ng E, Bhatia S, Trichter F, et al. 2D kV orthogonal imaging with fiducial markers is more precise for daily image guided alignments than soft-tissue cone beam computed tomography for prostate radiation therapy. Adv Radiat Oncol 2017;2:420–8.

[32] Berger T, Petersen JBB, Lindegaard JC, et al. Impact of bowel gas and body outline variations on total accumulated dose with intensity-modulated proton therapy in locally advanced cervical cancer patients. Acta Oncol 2017;56:1472–8.

[33] Kamnitsas K, Ledig C, Newcombe VFJ, et al. Efficient multi-scale 3D CNN with fully connected CRF for accurate brain lesion segmentation. Med Image Anal 2017;36:61–78.

[34] Huang G, Liu Z, Weinberger KQ. Densely connected convolutional networks. 2017 IEEE Conference on Computer Vision and Pattern Recognition (CVPR); 2017, 2261–2269.

[35] Dou QP, Yu L, Chen H, et al. 3D deeply supervised network for automated segmentation of volumetric medical images. Med Image Anal 2017;41:40–54.

[36] Milletari F, Navab N, Ahmadi S-A. V-Net: fully convolutional neural networks for volumetric medical image segmentation. 2016 Fourth International Conference on 3D Vision (3DV), 2016;565–571.

[37] Kilby W, Dooley JR, Kuduvalli G, et al. The cyberknife robotic radiosurgery system in 2010. Technol Cancer Res Treat 2010;9:433–52.